

Energy-Conserving Numerical Simulations of Electron Holes in Two-Species Plasmas

Yingda Cheng ^{*} Andrew J. Christlieb [†] Xinghui Zhong [‡]

March 18, 2014

Abstract

In this paper, we apply our recently developed energy-conserving discontinuous Galerkin (DG) methods [1] for the two-species Vlasov-Ampère system to simulate the evolution of electron holes (EHs). The EH is an important Bernstein-Greene-Kurskal (BGK) state and is constructed based on the Schamel distribution in our simulation. By varying the mass and temperature ratios, we observe the stationary and moving EHs, as well as the break up of EHs at later times upon initial perturbation of the electron distribution. Those results agree well with the existing results in the literature. Our methods are demonstrated to be conservative in the total energy and particle numbers for both species.

Keywords: Two-species Vlasov-Ampère system, energy conservation, discontinuous Galerkin methods, electron holes, Schamel distribution

1 Introduction

In this paper, we apply our recently developed energy-conserving discontinuous Galerkin (DG) methods [1] to simulate the evolution of electron holes (EHs) in two-species plasmas. In such multiscale dynamics, it is important not to introduce any artificial numerical heating or cooling to the electrons. Our methods can conserve the total particle number and total energy simultaneously regardless of the mesh size, and thus are suitable candidates for such simulations.

The objective of our numerical experiments is to study the nonlinear interactions of EHs with ions in the plasmas. The EH is an important Bernstein-Greene-Kurskal (BGK) state in plasmas, and represents electrons that are trapped in a self-created positive electrostatic potential. Such BGK-like states are observed experimentally in laboratory and space plasmas

^{*}Department of Mathematics, Michigan State University, East Lansing, MI 48824 U.S.A.
ycheng@math.msu.edu

[†]Department of Mathematics, Michigan State University, East Lansing, MI 48824 U.S.A.
christlieb@math.msu.edu

[‡]Department of Mathematics, Michigan State University, East Lansing, MI 48824 U.S.A.
zhongxh@math.msu.edu

and studied numerically since decades ago. For a complete reference, one can refer to the review paper [4]. In this paper, we will use an initial configuration of EHs constructed based on the Schamel distribution [9, 7, 8]. By varying the mass and temperature ratios between electrons and ions, the EH can develop quite different structures later on. We focus on two case scenarios, one with smaller EH speed and another with EH speed on the order of the ion-acoustic speed. The first was observed to sustain the stationary and moving EH holes [3], while the second causes wave transformations [6].

Our model equation under consideration is the two-species non-relativistic Vlasov-Ampère (VA) system for electrons and ions. Under the scaling that density, time and space variables are in units of the background electron number density n_0 , the electron plasma period $\omega_{pe}^{-1} = \left(\frac{n_0 e^2}{\varepsilon_0 m_e}\right)^{-1/2}$ and the electron Debye radius $\lambda_{De} = \left(\frac{\varepsilon_0 k_B T_e}{n_0 e^2}\right)^{1/2}$, respectively, the distribution function f_α is scaled by n_0/V_{T_e} , where $V_{T_e} = (k_B T_e/m_e)^{1/2}$ is the electron thermal speed, T_e is the electron temperature; the electric field E and the current density are scaled by $k_B T_e/e\lambda_{De}$ and $n_0 e V_{T_e}$, we arrive at the dimensionless equations

$$\partial_t f_\alpha + \mathbf{v} \cdot \nabla_{\mathbf{x}} f_\alpha + \mu_\alpha \mathbf{E} \cdot \nabla_{\mathbf{v}} f_\alpha = 0, \quad (\mathbf{x}, \mathbf{v}) \in (\Omega_x, \mathbb{R}^n), \quad \alpha = e, i \quad (1.1a)$$

$$\partial_t \mathbf{E} = -\mathbf{J}, \quad \mathbf{x} \in \Omega_x \quad (1.1b)$$

where Ω_x is the physical domain, $\alpha = e, i$, e for electrons and i for ions, $\mu_\alpha = \frac{q_\alpha m_e}{e m_\alpha}$, i.e. $\mu_e = -1$, $\mu_i = \frac{m_e}{m_i}$. $\mathbf{J} = \mathbf{J}_i - \mathbf{J}_e$, with $\mathbf{J}_\alpha = \int_{\mathbb{R}^n} f_\alpha(\mathbf{x}, \mathbf{v}, t) \mathbf{v} d\mathbf{v}$. Our numerical method [1] is verified to preserve the total particle number for each species $\int_{\Omega_x} \int_{\mathbb{R}^n} f_\alpha d\mathbf{v} d\mathbf{x}$, $\alpha = e, i$, and the total energy

$$TE = \frac{1}{2} \int_{\Omega_x} \int_{\mathbb{R}^n} f_e |\mathbf{v}|^2 d\mathbf{v} d\mathbf{x} + \frac{1}{2\mu_i} \int_{\Omega_x} \int_{\mathbb{R}^n} f_i |\mathbf{v}|^2 d\mathbf{v} d\mathbf{x} + \frac{1}{2} \int_{\Omega_x} |\mathbf{E}|^2 d\mathbf{x}.$$

The rest of this paper is organized as follows: in Section 2, we review the energy-conserving schemes developed in [1]. Section 3 is devoted to numerical simulations of EHs. We specify the numerical parameters and the initial conditions, and discuss the behaviors of EHs in those two cases. Finally, we conclude with a few remarks in Section 4.

2 Numerical Algorithms

In this section, we highlight the numerical algorithms used to discretize the two-species VA system (1.1). For complete details of the methods as well as their properties, we refer the readers to [1].

Our numerical discretizations use two types of time stepping algorithms: one is the

explicit method denoted by **Scheme-1**(Δt) given as follows

$$\frac{f_\alpha^{n+1/2} - f_\alpha^n}{\Delta t/2} + \mathbf{v} \cdot \nabla_{\mathbf{x}} f_\alpha^n + \mu_\alpha \mathbf{E}^n \cdot \nabla_{\mathbf{v}} f_\alpha^n = 0, \quad \alpha = e, i \quad (2.2a)$$

$$\frac{\mathbf{E}^{n+1} - \mathbf{E}^n}{\Delta t} = -\mathbf{J}^{n+1/2}, \quad \text{where } \mathbf{J}^{n+1/2} = \int_{\mathbb{R}^n} (f_i^{n+1/2} - f_e^{n+1/2}) \mathbf{v} d\mathbf{v} \quad (2.2b)$$

$$\frac{f_\alpha^{n+1} - f_\alpha^n}{\Delta t} + \mathbf{v} \cdot \nabla_{\mathbf{x}} f_\alpha^{n+1/2} + \frac{1}{2} \mu_\alpha (\mathbf{E}^n + \mathbf{E}^{n+1}) \cdot \nabla_{\mathbf{v}} f_\alpha^{n+1/2} = 0. \quad (2.2c)$$

The other is the implicit scheme using the splitting approach. Namely, we define

$$\frac{f_\alpha^{n+1} - f_\alpha^n}{\Delta t} + \mathbf{v} \cdot \nabla_{\mathbf{x}} \frac{f_\alpha^n + f_\alpha^{n+1}}{2} = 0, \quad (2.3a)$$

$$\frac{\mathbf{E}^{n+1} - \mathbf{E}^n}{\Delta t} = 0, \quad (2.3b)$$

as **Scheme-a**(Δt) as in [1], and

$$\frac{f_\alpha^{n+1} - f_\alpha^n}{\Delta t} + \frac{1}{2} \mu_\alpha (\mathbf{E}^n + \mathbf{E}^{n+1}) \cdot \nabla_{\mathbf{v}} \frac{f_\alpha^n + f_\alpha^{n+1}}{2} = 0, \quad \alpha = e, i \quad (2.4a)$$

$$\frac{\mathbf{E}^{n+1} - \mathbf{E}^n}{\Delta t} = -\frac{1}{2} (\mathbf{J}^n + \mathbf{J}^{n+1}), \quad (2.4b)$$

as **Scheme-b**(Δt) as in [1]. Then the fully implicit method is given by Strang Splitting

$$\mathbf{Scheme-2}(\Delta t) := \mathbf{Scheme-a}(\Delta t/2) \mathbf{Scheme-b}(\Delta t) \mathbf{Scheme-a}(\Delta t/2).$$

Those second-order accurate time discretizations coupled with DG finite element methods in (\mathbf{x}, \mathbf{v}) space yield fully discrete methods that are total particle number and energy-conserving when quadratic and above polynomials are used in the phase space. A side remark is that a truncation of the velocity domain is necessary for the numerical computation. In particular, we denote Ω_{v_α} , $\alpha = e, i$ to be the truncated velocity domain for electrons and ions. We assume that such domains are taken large enough, so that the distribution functions vanish on the velocity boundary.

3 Simulation Results

In this section, we discuss the simulation results. In particular, two cases are considered. One set of simulations follows [3] with $T_e/T_i = 1$, and $m_i/m_e = 29500$. Another set of simulations follows [6] with $T_e/T_i = 40$ and $m_i/m_e = 100$. They demonstrate quite different behaviors as detailed in Section 3.2.2 .

3.1 Initial conditions

In our numerical experiments, the initial condition of the electron distribution f_e is set to be the Schamel distribution [9] for the free and trapped electrons, which in the rest frame of the bulk plasma has the form

$$f_e = \begin{cases} \frac{1}{\sqrt{2\pi}} \exp\left(-\frac{1}{2}[(|v - M|^2 - 2\phi)^{\frac{1}{2}} + M]^2\right), & v - M > \sqrt{2\phi} \\ \frac{1}{\sqrt{2\pi}} \exp\left(-\frac{1}{2}[-(|v - M|^2 - 2\phi)^{\frac{1}{2}} + M]^2\right), & v - M < -\sqrt{2\phi} \\ \frac{1}{\sqrt{2\pi}} \exp\left(-\frac{1}{2}[\beta((v - M)^2 - 2\phi) + M^2]\right), & |v - M| \leq \sqrt{2\phi} \end{cases} \quad (3.5)$$

where M is the mach number (the speed of the electron hole) and β is the trapping parameter [7, 8]. The initial condition for the ion distribution function f_i is taken to be the Maxwellian distribution

$$f_i = \frac{1}{\sqrt{2\pi\gamma}} e^{-v^2/2\gamma}, \quad (3.6)$$

where $\gamma = T_i m_e / T_e m_i$. After integrating the untapped and trapped electrons over velocity space [9], we get the electron density

$$\rho_e = e^{-M^2/2} \left\{ I(\phi) + \kappa\left(\frac{M^2}{2}, \phi\right) + \frac{2}{\sqrt{\pi|\beta|}} W_D\left(\sqrt{-\beta\phi}\right) \right\}, \quad (3.7)$$

where

$$I(x) = e^x (1 - \operatorname{erf}(\sqrt{x})), \quad (3.8a)$$

$$\kappa(x, y) = \frac{2}{\sqrt{\pi}} \int_0^{\pi/2} \sqrt{x} \cos \psi \exp(-y \tan^2(\psi) + x \cos^2(\psi)) \operatorname{erf}(\sqrt{x} \cos \psi) d\psi, \quad (3.8b)$$

$$w_D(x) = e^{-x^2} \int_0^x e^{t^2} dt. \quad (3.8c)$$

Clearly, $\rho_i = 1$. Poisson's equation with ρ_e given by (3.7), is solved as a nonlinear boundary value problem, where ϕ is set to zero far away on each side of the EH. A central difference approximation is used for the second derivative in Poisson's equation, leading to a system of nonlinear equations, which is solved iteratively with Newton's method. The potential obtained (and fitted into a piecewise quadratic polynomial) is then inserted in to (3.5) to obtain the electron distribution. In Figure 3.1, we plot the EH electric potential and electron density for different M and β . We note that larger values of M and $|\beta|$ give smaller maxima of the potential and less deep electron density minima, in agreement with Figure 1 in [3]. In particular, we measure the maximum and half width of the potential for $M = 0, \beta = -0.7$ to be 4.02 and 4.61, $M = 0, \beta = -0.5$ to be 7.37 and 4.48.

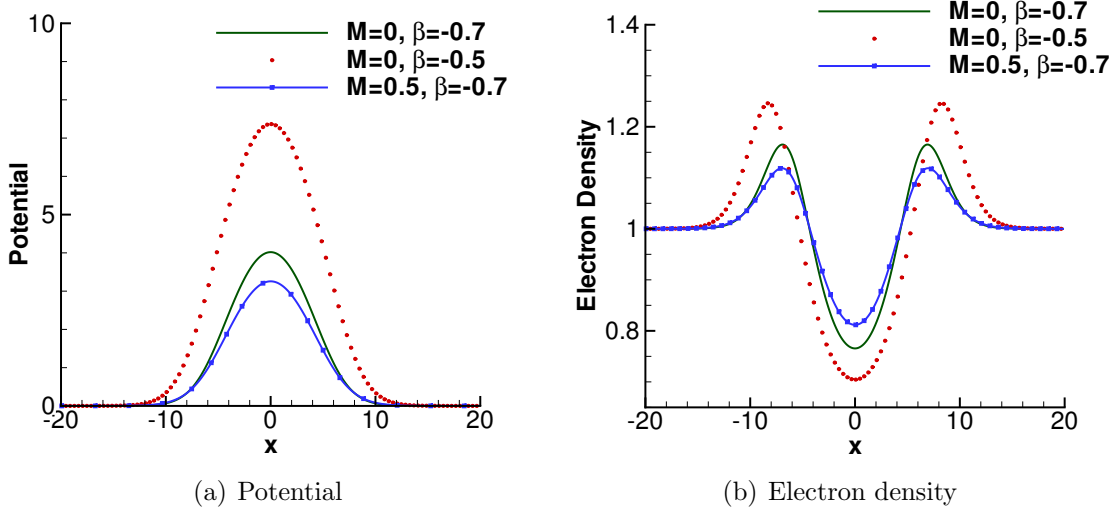


Figure 3.1: The potential and the electron density, associated with a standing electron hole ($M = 0$) with the trapping parameters $\beta = -0.7$ (solid lines) and $\beta = -0.5$ (dotted lines), and a moving electron hole with $M = 0.5$ and $\beta = -0.7$ (lines with square symbols) in plasmas with fixed ion background ($N_i = 1$).

We also use the potentials obtained in Figure 3.1 to construct the numerical initial conditions for the electron and ion distribution functions of EHs. Following [3], in our simulations, we test the following three initial conditions as perturbed state of the Schamel distribution. By adding the small perturbations, we will be able to study the stability properties of the EHs in those three settings.

- (1) Single EH with $\beta = -0.7$. We take $M = 0$ and $\beta = -0.7$ (the solid line in Figure 3.1), with a small local perturbation of the plasma near the EH. The perturbation consists of a Maxwellian distribution of electrons added to the initial condition for the electron hole, with the same temperature as the background electrons and with density perturbation of the form $\delta\rho_e = -0.008 \sinh(x/2) / \cosh^2(x/2)$.
- (2) Single EH with $\beta = -0.5$. We take $M = 0$ and $\beta = -0.5$ (the dotted line in Figure 3.1), corresponding to a larger EH and the same perturbations with density perturbation of the form $\delta\rho_e = 0.008 \sinh(x/2) / \cosh^2(x/2)$.
- (3) Two EHs. In this case, two EHs with $\beta = -0.5$ and $\beta = -0.7$ are initially placed at $x = -40$ and $x = 40$, respectively. A local electron density perturbation is taken to be Maxwellian with the density

$$\delta\rho_e = 0.08 \left(\sinh((x + 40)/2) / \cosh^2((x + 40)/2) - \sinh((x - 40)/2) / \cosh^2((x - 40)/2) \right).$$

We run four numerical simulations with the parameters described as follows.

Run 1 $T_e/T_i = 1$, and $m_i/m_e = 29500$. Single EH with $\beta = -0.7$. $\Omega_x = [-130, 30]$. $\Omega_{v_e} = [-15.7, 15.7]$, $\Omega_{v_i} = [-0.118, 0.118]$.

Run 2 $T_e/T_i = 1$, and $m_i/m_e = 29500$. Single EH with $\beta = -0.5$. $\Omega_x = [-20, 140]$. $\Omega_{v_e} = [-15.7, 15.7]$, $\Omega_{v_i} = [-0.118, 0.118]$.

Run 3 $T_e/T_i = 1$, and $m_i/m_e = 29500$. Two EHs. $\Omega_x = [-80, 80]$. $\Omega_{v_e} = [-15.7, 15.7]$, $\Omega_{v_i} = [-0.118, 0.118]$.

Run 4 $T_e/T_i = 40$ and $m_i/m_e = 100$. Single EH with $\beta = -0.7$. $\Omega_x = [-80, 80]$. $\Omega_{v_e} = [-15.7, 15.7]$, $\Omega_{v_i} = [-1, 1]$.

We take a mesh of uniform $N_x = 512$ cells in the x direction, and $N_v = N_{v,e} = N_{v,i} = 300$ cells in the v direction for all runs. Quadratic polynomial spaces are used in the phase space. For the explicit method **Scheme-1**, we take CFL to be 0.13 due to the stability restriction, while for **Scheme-2**, CFL is taken to be 10. For **Scheme-2**, we use KINSOL from SUNDIALS [5] to solve the nonlinear algebraic systems with the tolerance parameter set to be $\epsilon_{tol} = 10^{-11}$. We notice that the conservation results will depend on the size of $\Omega_{v_e}, \Omega_{v_i}$, and the tolerance parameter [1]. Another remark is that our schemes can easily handle nonuniform grids, and higher order polynomials can be used in the calculations to reduce numerical diffusion, but we do not pursue them in this paper.

3.2 Discussion of simulation results

3.2.1 Conservation properties

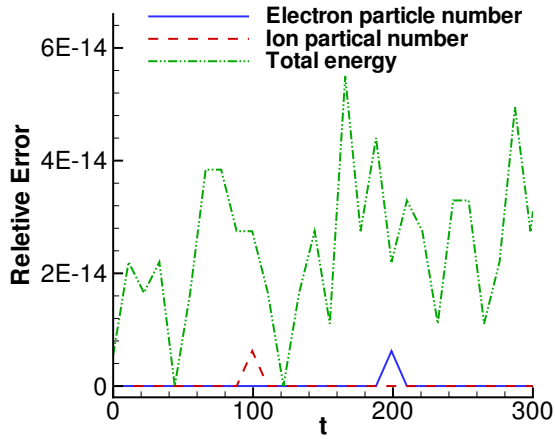
First, we verify the conservation properties of the numerical methods for the above four simulations. Figures 3.2 and 3.3 show the absolute value of relative errors of the total particle number and total energy for our four simulations with **Scheme-1** and **Scheme-2**. The total time is chosen corresponding to the feature of each simulation, which will be discussed later in details. We can see that most errors stay small, below 10^{-12} for the whole duration of the simulations for **Scheme-1** and below 10^{-9} for **Scheme-2**. The errors of total energy for **Scheme-2** are slightly larger mainly due to the error caused by the Newton-Krylov solver relating to the preset tolerance parameter $\epsilon_{tol} = 10^{-11}$. Because of the slightly larger variations in the conservation, the errors for **Scheme-2** are plotted in the log scale, compared to the normal scale used for **Scheme-1**. The simulation results validate the excellent conservation properties of our numerical schemes.

3.2.2 Evolutions of EHs

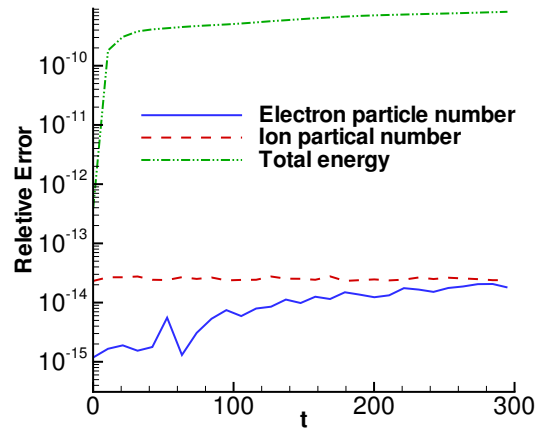
Next, we will provide interpretation of the four numerical runs. To save space, we only show results of one scheme for each case. For runs 1 and 3, we use the explicit method **Scheme-1**, while for runs 2 and 4, we use the implicit method **Scheme-2**. For all the contour figures below, we zoom in velocity space in order to see the details of the distribution functions.

Run 1

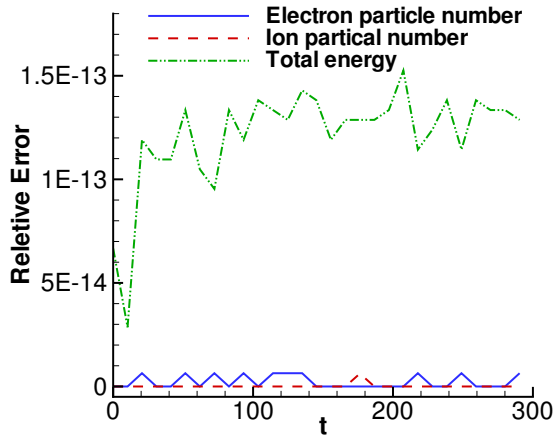
In Figure 3.4, we show the time evolution of the electron density, the ion density, the electric field and the potential of an initially stationary electron hole. The results agree well with the simulations obtained in [3] by the Fourier transformed methods [2]. In particular, we observe that the EH starts moving in the negative x direction at $t \in [130, 140]$ with a



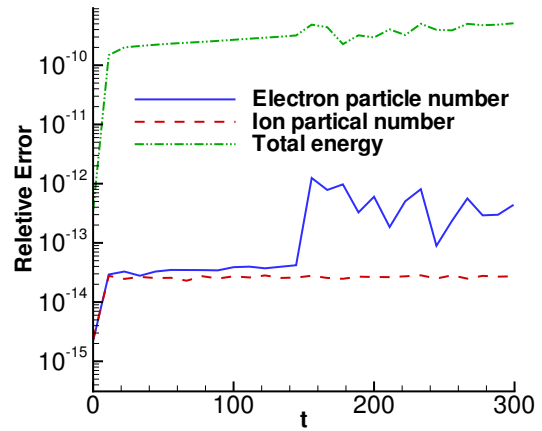
(a) Scheme-1. Run 1.



(b) Scheme-2. Run 1.

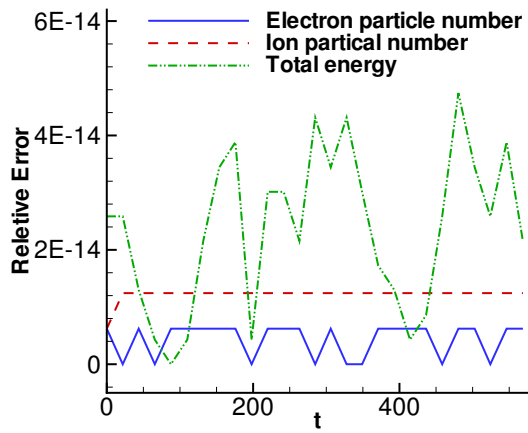


(c) Scheme-1. Run 2.

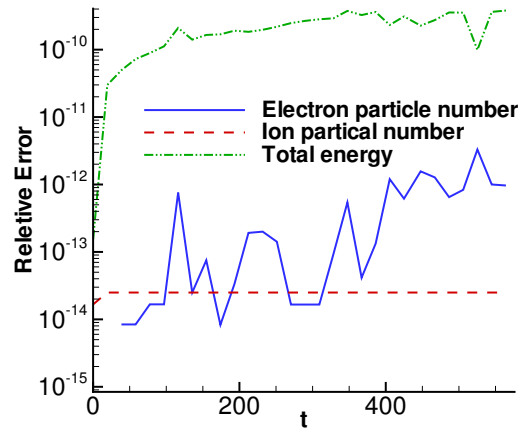


(d) Scheme-2. Run 2.

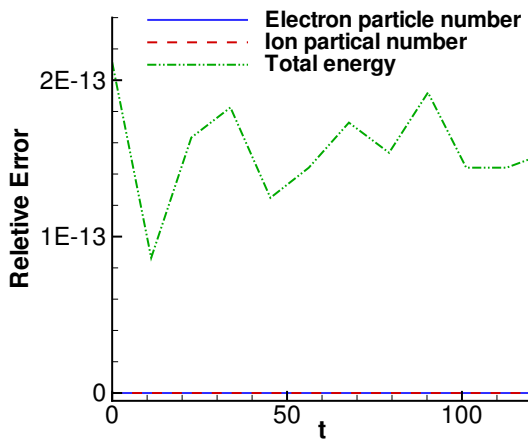
Figure 3.2: Evolution of absolute value of relative errors in total particle number and total energy. Runs 1 & 2.



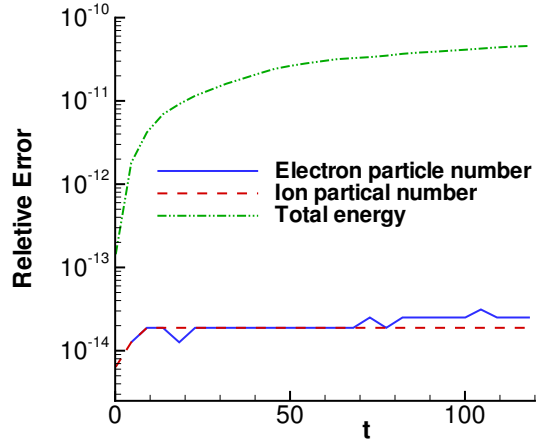
(a) **Scheme-1.** Run 3.



(b) **Scheme-2.** Run 3.



(c) **Scheme-1.** Run 4



(d) **Scheme-2.** Run 4

Figure 3.3: Evolution of absolute value of relative errors in total particle number and total energy. Runs 3 & 4.

Mach number $M \approx 0.55$. This sudden acceleration can be explained by the cavity in the ion density that has built up and made the EH unstable. After $t \approx 140$, ion density cavity continues to deepen and an electron density cavity is created at the same place, neutralizing the plasma. In Figure 3.5, we plot the electron and ion distributions at $t = 0$, the initial condition and $t = 200$ when the EH has moved to $x \approx -40$. We confirm the observation made in Figure 3.4 about the behavior of the distribution functions for both species.

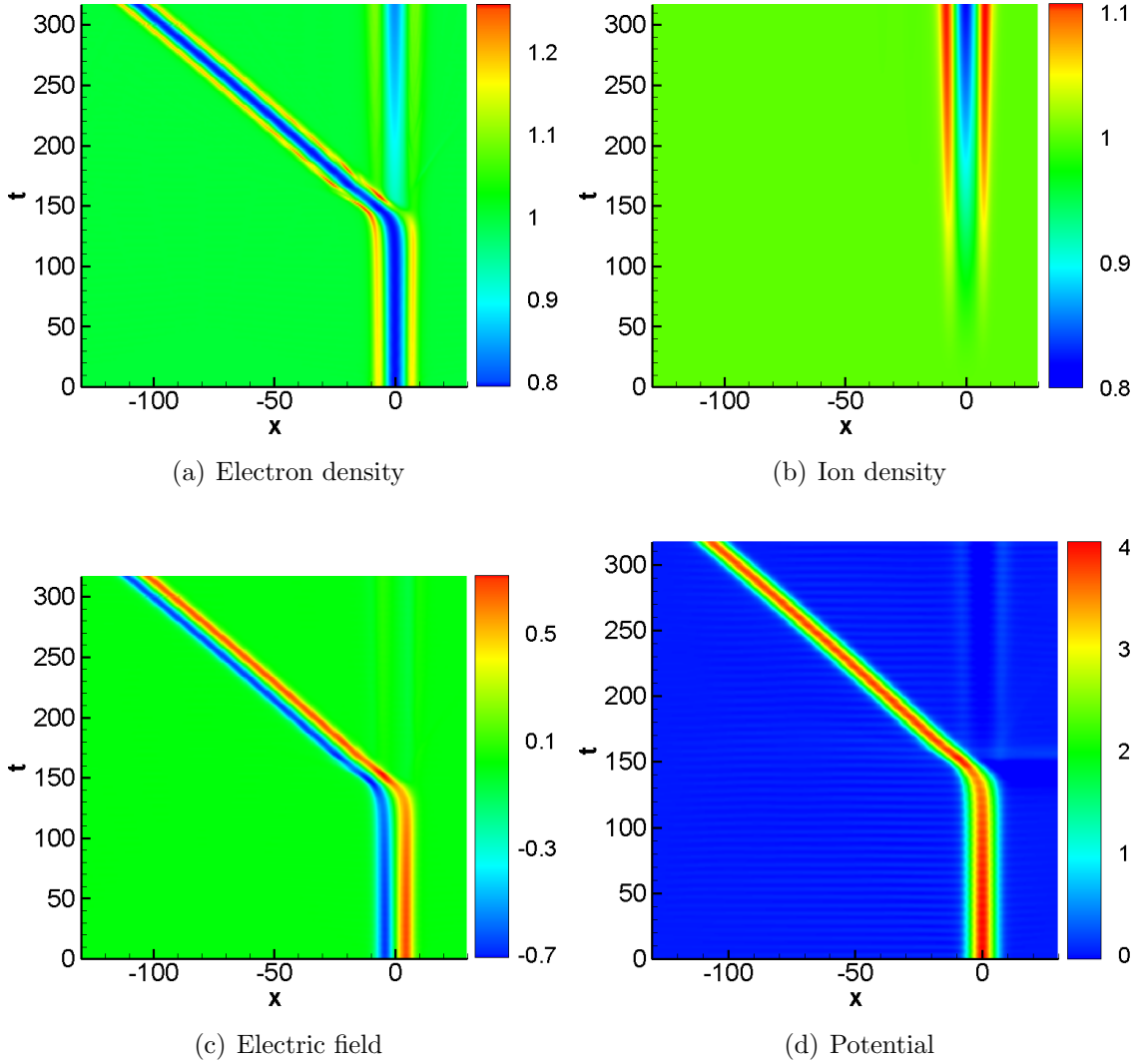


Figure 3.4: Evolution of the electron density, the ion density, the electric field and the potential of Run 1. **Scheme-1.**

Run 2

This simulation has qualitatively similar results as the first run. Notice that due to the difference in the sign of the perturbation, the direction of propagation of the EH is reversed to the positive x direction. In Figure 3.6, we show the time development of this EH. In

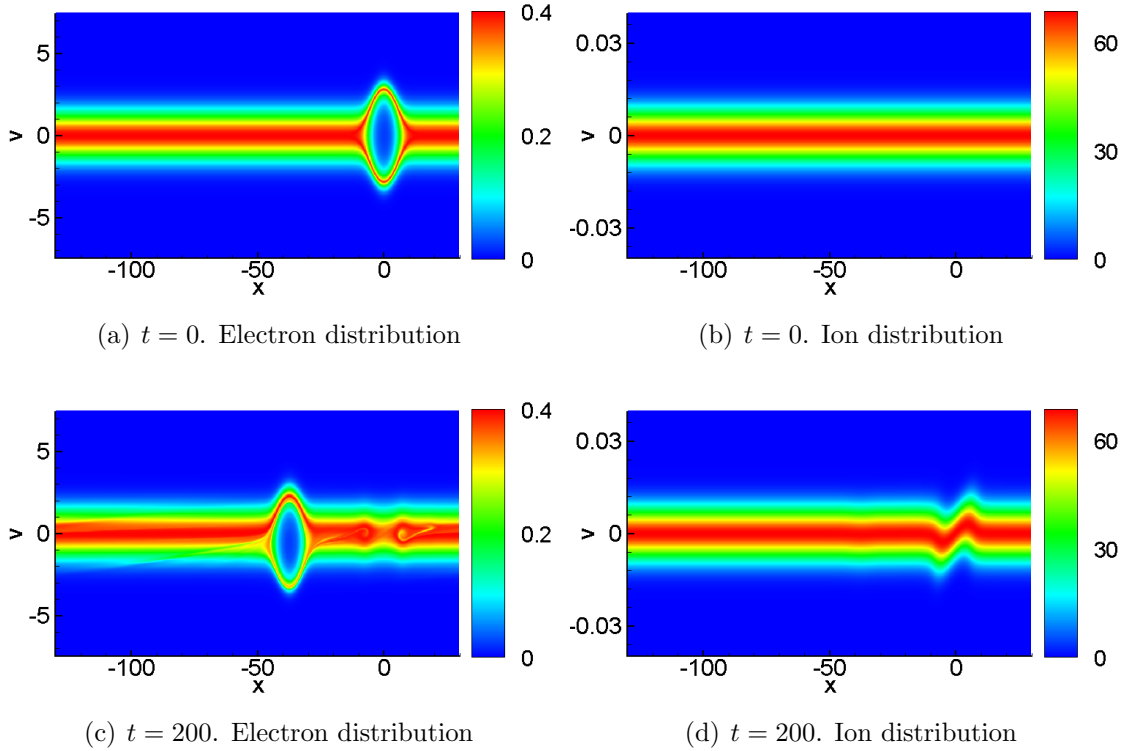


Figure 3.5: Contour plots of the electron and ion distributions of Run 1. **Scheme-1.**

this case, the EH starts moving after $t \in [120, 130]$ also with a Mach number $M \approx 0.55$. In Figure 3.7, we plot the electron and ion distributions at $t = 0$, the initial condition and $t = 200$ when the EH has moved to $x \approx 60$.

Run 3

In this run, we study interactions between two EHs with each other and with ions in a longer simulation. The EHs with $\beta = -0.5$ and $\beta = -0.7$ are initially placed at $x = -40$ and $x = 40$, respectively. We obtain qualitatively similar results to [3]. In Figure 3.8, we observe stationary EHs until sufficient ion density cavities have built up, up to $t \approx 110$ and $t \approx 130$, respectively for the two EHs. Then merging of the two EHs occur at $t \approx 170$, whereafter the single EH propagates slightly in the positive x direction, and becomes trapped at a local ion density maximum at $x \approx 30$. More interesting, after $t \approx 400$, a new ion density cavity is created where the EH is centered, and at this time the EH is again accelerated in the negative x direction. At $t \approx 480$, the moving EH again encounters an ion density maximum located at $x \approx -30$, where the EH is trapped, performing large oscillations. We confirm our observations by plotting the electron and ion phase space density in Figures 3.9 and 3.10, where we consider the initial condition ($t = 0$), the two EHs that move ($t = 155$), collisions between the two EHs ($t = 175$), the newly created EH trapped at $x \approx 30$ ($t = 251$), and the EH trapped at $x \approx -30$ ($t = 481, 576$).

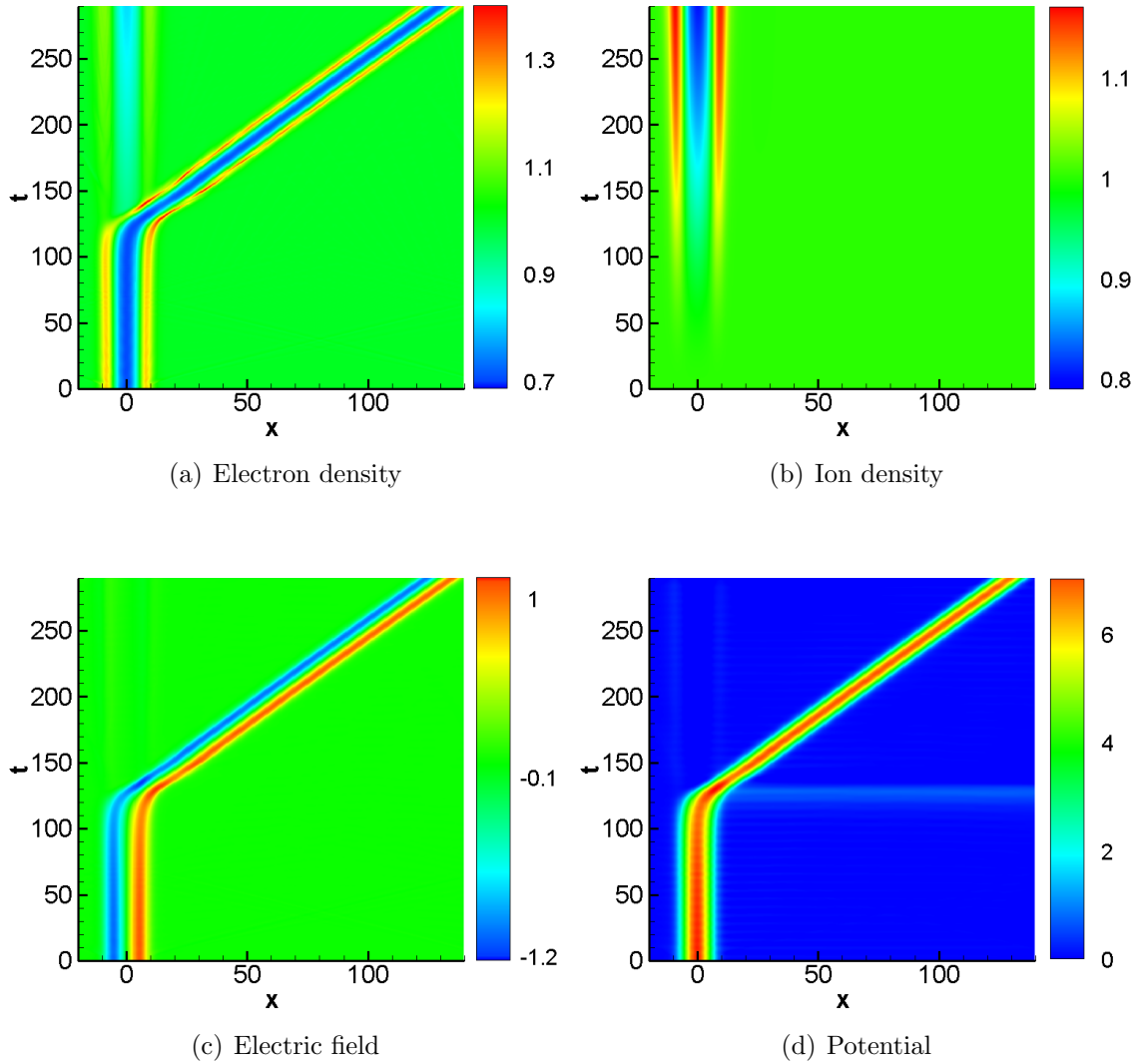


Figure 3.6: Evolution of the electron density, the ion density, the electric field and the potential of Run 2. **Scheme-2**.

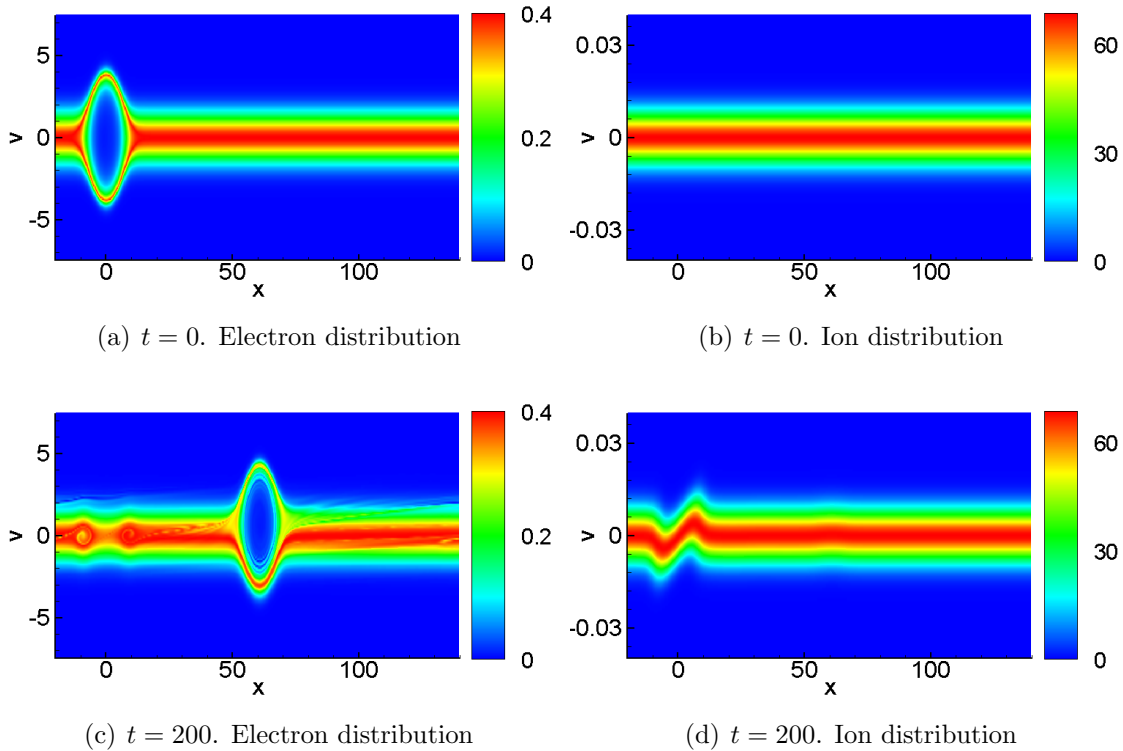


Figure 3.7: Contour plots of the electron and ion distributions of Run 2. **Scheme-2.**

Run 4

This run involves EHs that are unstable and wave transformations are present. Figure 3.11 plots the evolution of the electron density, the ion density, the electric field and the potential. We can clearly observe the creation of two EHs after $t \approx 25$. In fact, the electron and ion distributions depicted in Figures 3.12 and 3.13 are very illuminating. Figure 3.12 shows the initial formation of the two EHs up to $t = 50$. Those two EHs seem to stay unstable at later times as shown in Figure 3.13. The main reason for this different behavior compared to previous runs is due to the choice of mass and temperature ratios, making the EH speed comparable to the ion-acoustic speed, causing the EH to transform and break up. We notice such unstable behaviors are also observed in [6] for a large EH initially placed at $x = 0$.

4 Conclusion

In this paper, we use the energy-conserving schemes to simulate the time evolution of EHs. We verify the behaviors of EHs corresponding to different mass and temperature ratios. Our methods are demonstrated to be conservative in particle number and total energy. Numerical results of high fidelity are produced matching those in the literature.

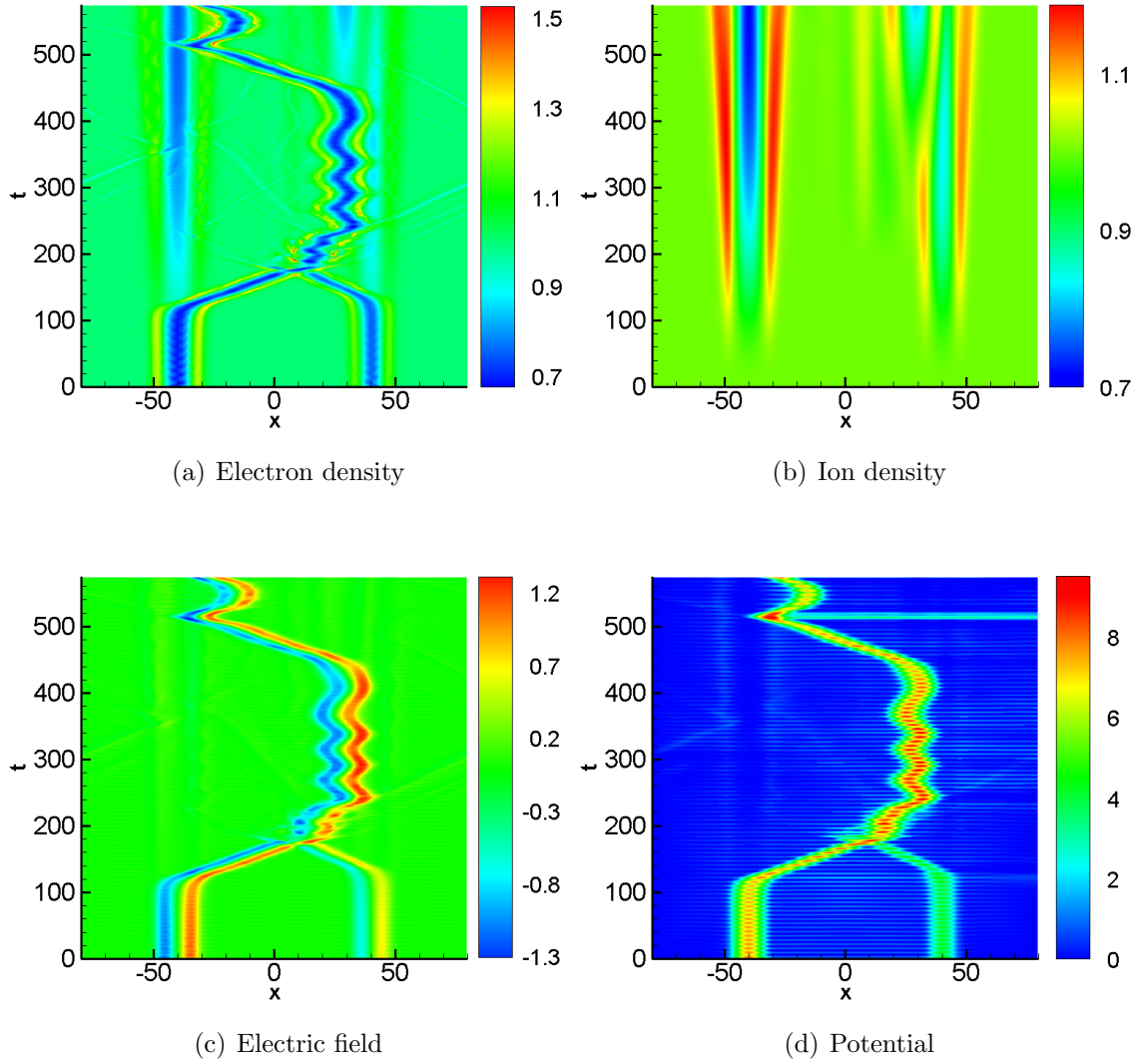


Figure 3.8: Evolution of the electron density, the ion density, the electric field and the potential of Run 3. **Scheme-1**.

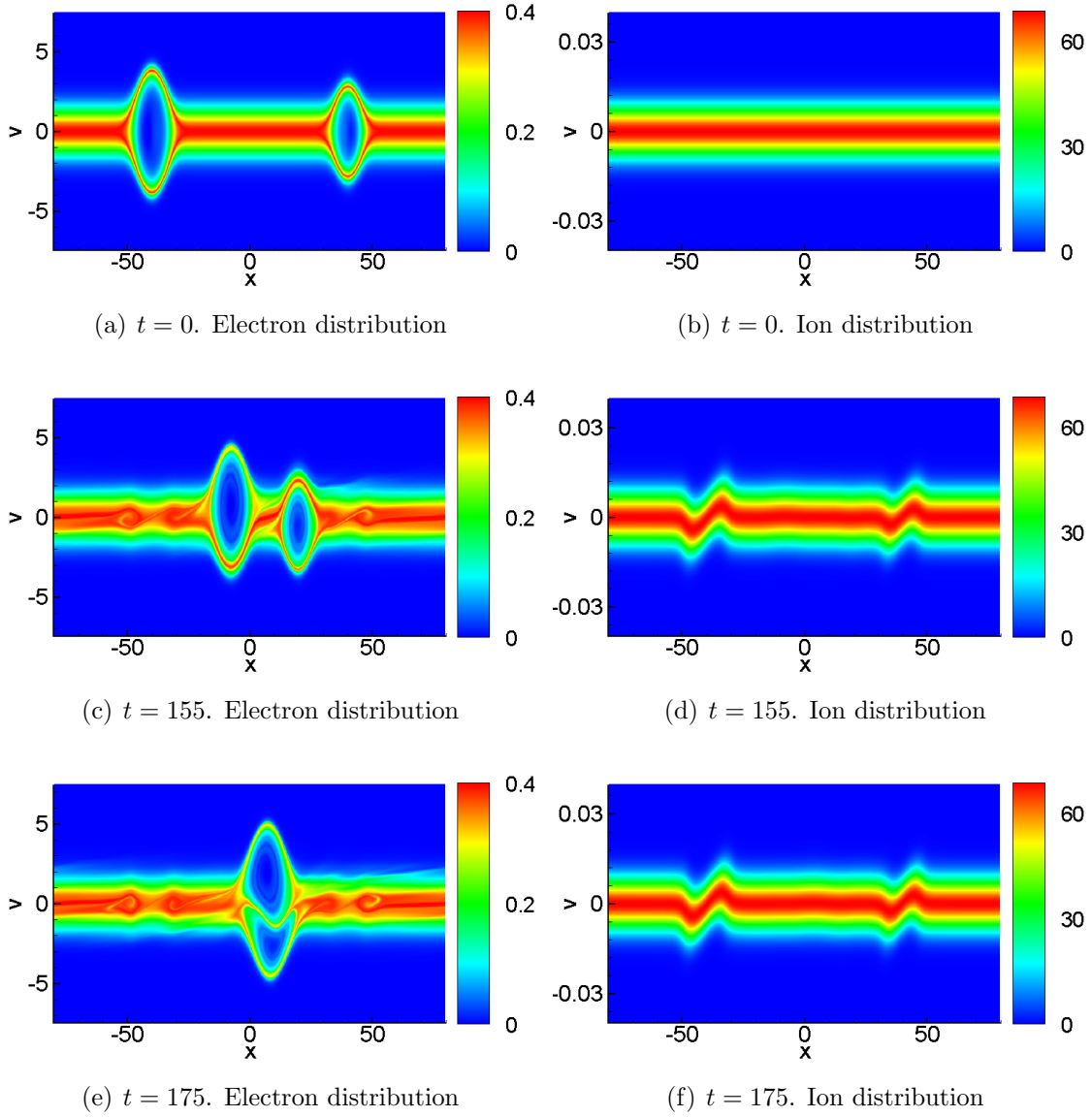


Figure 3.9: Contour plots of the electron and ion distributions of Run 3. **Scheme-1.**

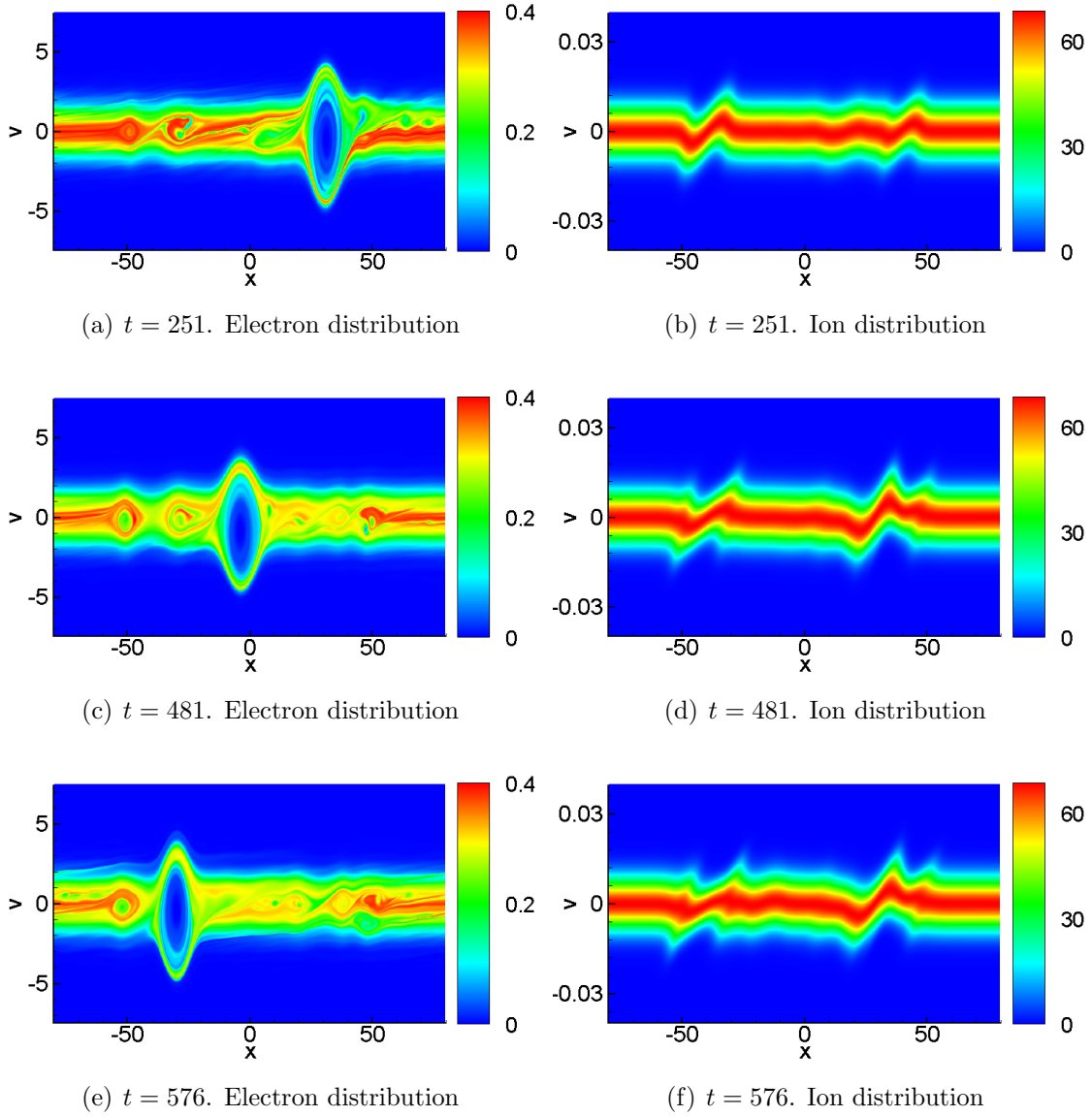


Figure 3.10: Contour plots of the electron and ion distributions of Run 3. **Scheme-1.**

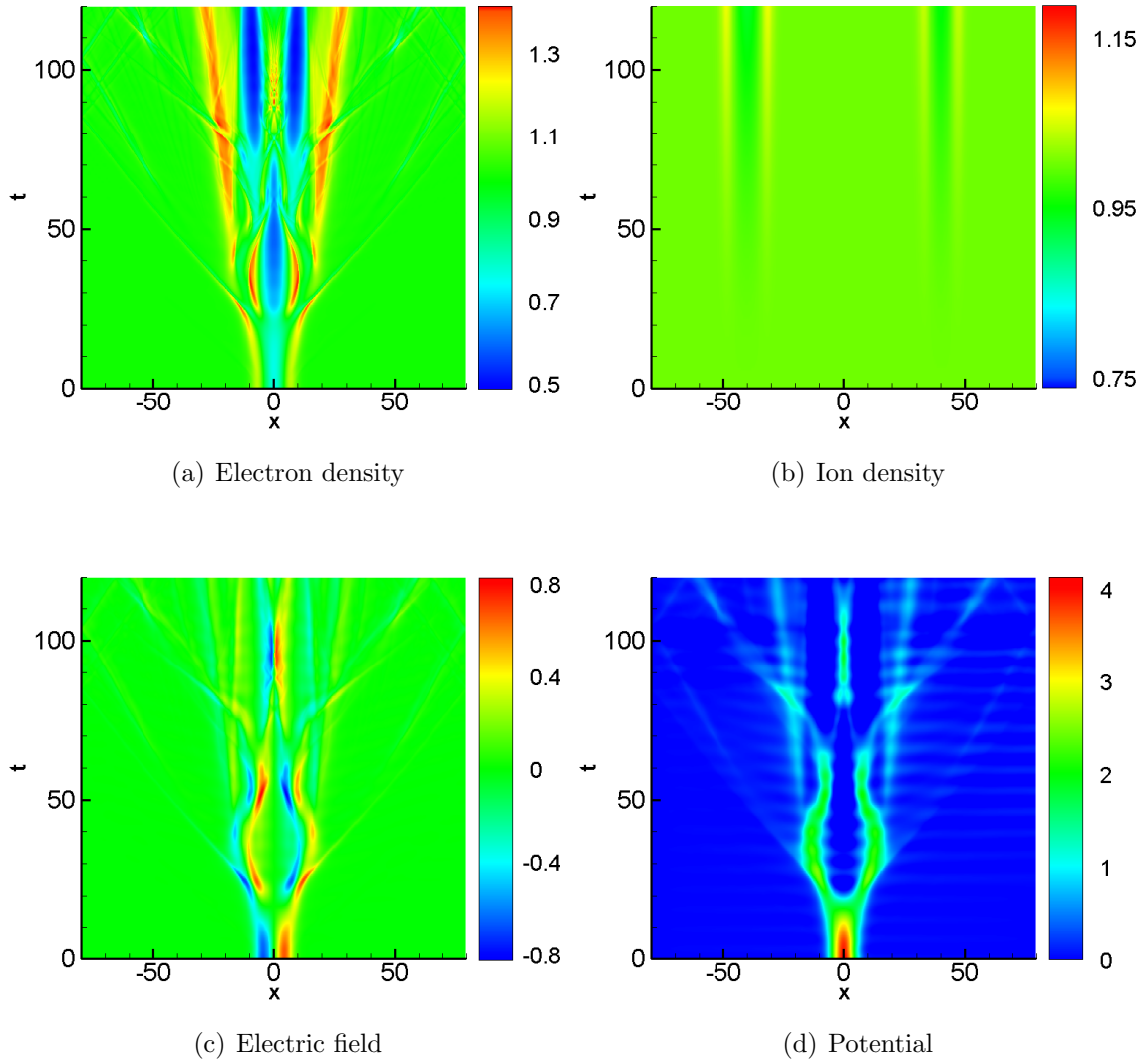


Figure 3.11: Evolution of the electron density, the ion density, the electric field and the potential of Run 4. **Scheme-2**.

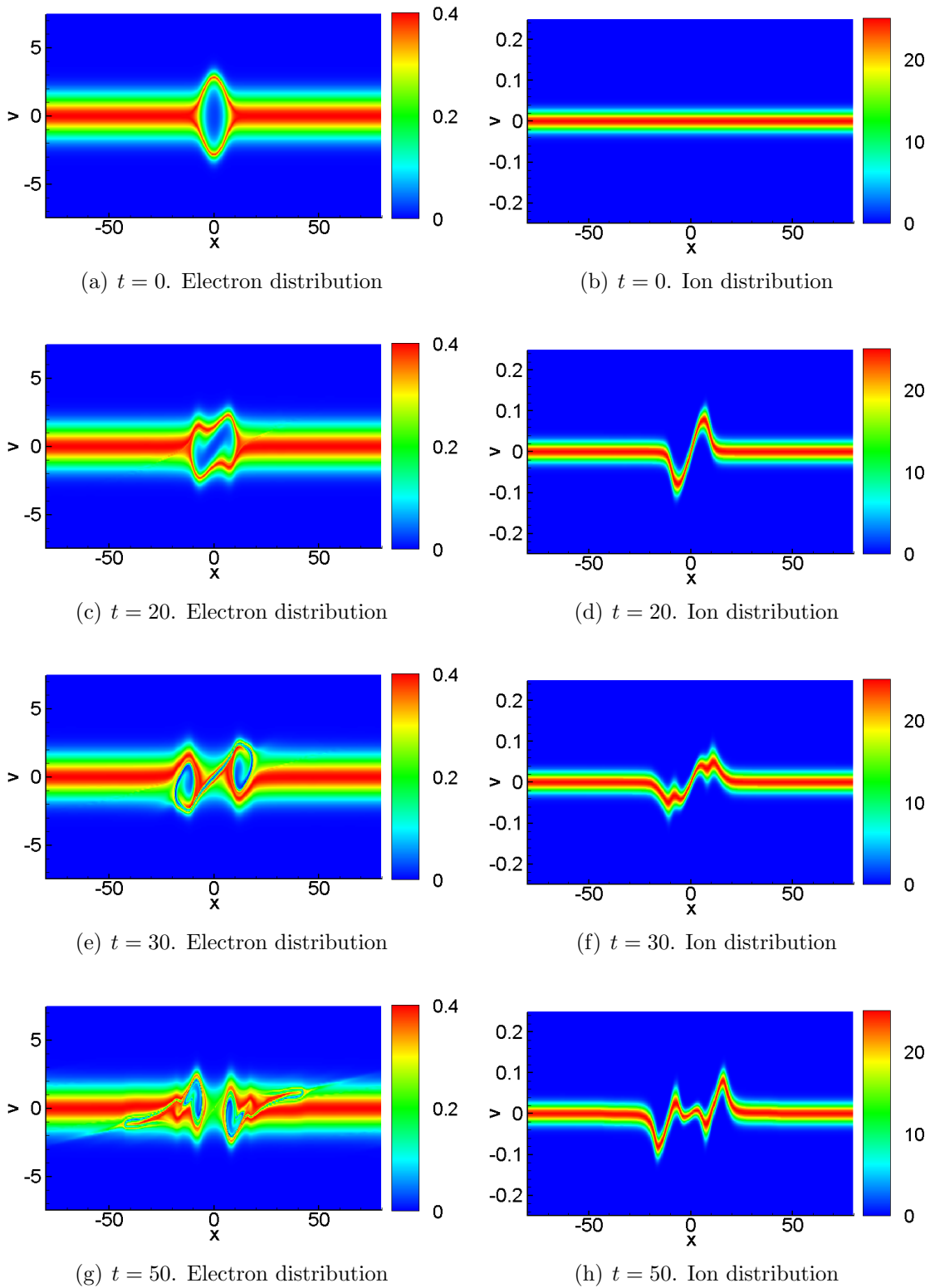


Figure 3.12: Contour plots of the electron and ion distributions of Run 4. **Scheme-2.**

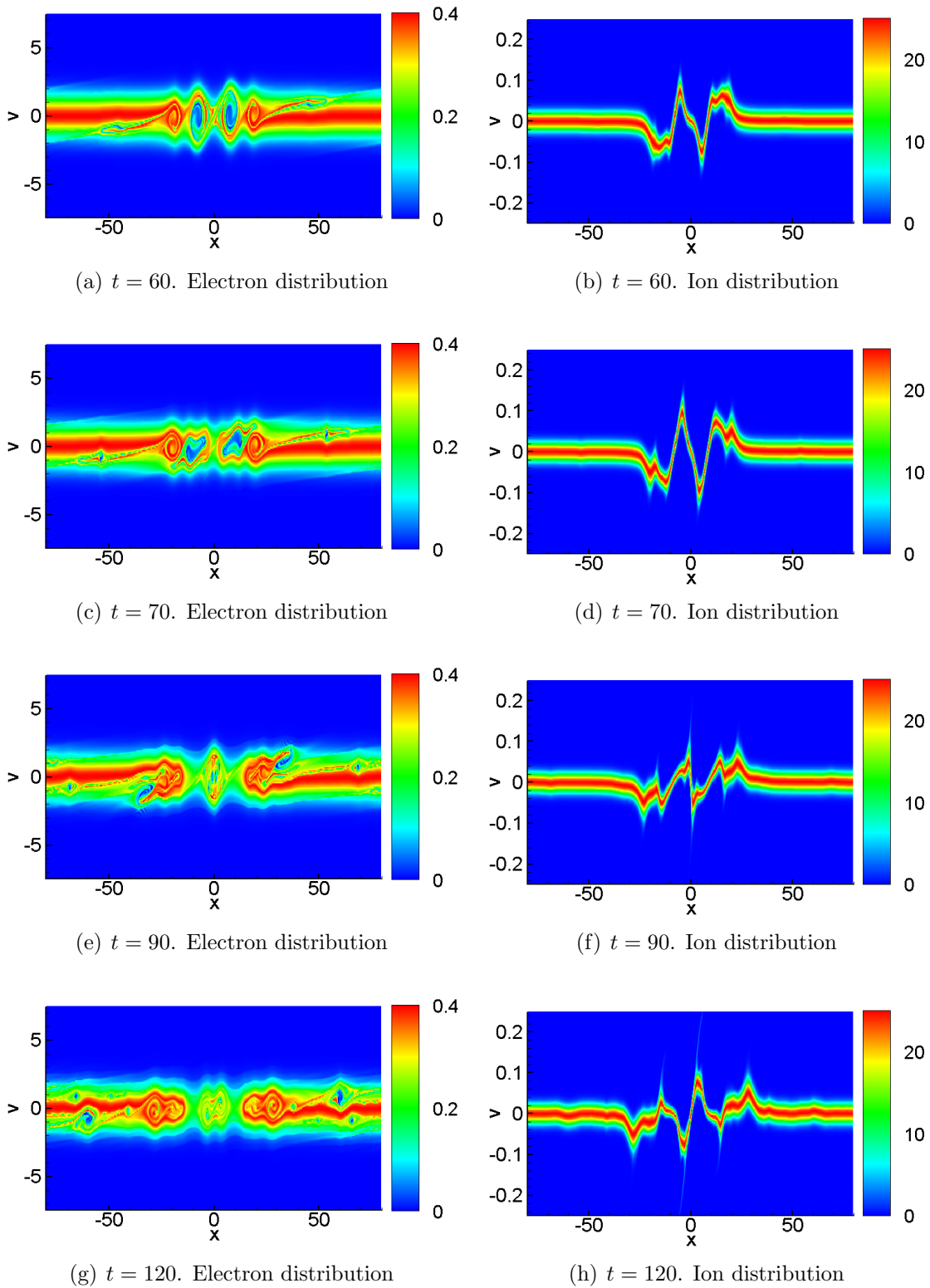


Figure 3.13: Contour plots of the electron and ion distributions of Run 4. **Scheme-2.**

Acknowledgments

YC is supported by grants NSF DMS-1217563, DMS-1318186, AFOSR FA9550-12-1-0343 and the startup fund from Michigan State University. AJC is supported by AFOSR grants FA9550-11-1-0281, FA9550-12-1-0343 and FA9550-12-1-0455, NSF grant DMS-1115709 and MSU foundation SPG grant RG100059. We gratefully acknowledge the support from Michigan Center for Industrial and Applied Mathematics.

References

- [1] Y. Cheng, A. J. Christlieb, and X. Zhong. Numerical Study of the Two-Species Vlasov–Ampère System: Energy-Conserving Schemes and the Current-Driven Ion-Acoustic Instability. 2014.
- [2] B. Eliasson. Numerical modelling of the two-dimensional Fourier transformed Vlasov–Maxwell system. *Journal of Computational Physics*, 190(2):501–522, 2003.
- [3] B. Eliasson and P. K. Shukla. Dynamics of electron holes in an electron-oxygen-ion plasma. *Phys. Rev. Lett.*, 93:045001, Jul 2004.
- [4] B. Eliasson and P. K. Shukla. Formation and dynamics of coherent structures involving phase-space vortices in plasmas. *Physics reports*, 422(6):225–290, 2006.
- [5] A. C. Hindmarsh, P. N. Brown, K. E. Grant, S. L. Lee, R. Serban, D. E. Shumaker, and C. S. Woodward. Sundials: Suite of nonlinear and differential/algebraic equation solvers. *ACM T. Math. Software*, 31(3):363–396, 2005.
- [6] K. Saeki and H. Genma. Electron-hole disruption due to ion motion and formation of coupled electron hole and ion-acoustic soliton in a plasma. *Physical review letters*, 80(6):1224, 1998.
- [7] H. Schamel. Stationary solutions of the electrostatic vlasov equation. *Plasma Physics*, 13:491–506, 1971.
- [8] H. Schamel. Stationary solitary, snoidal and sinusoidal ion acoustic waves. *Plasma Physics*, 14:905–924, 1972.
- [9] H. Schamel. Theory of electron holes. *Physica Scripta*, 20:336–342, 1979.